12-2008

Resonant Ultrasound Studies of Quasi-2D Na_xCoO_2

Timothy Allen Cagle
University of Tennessee - Knoxville

To the Graduate Council:

I am submitting herewith a thesis written by Timothy Allen Cagle entitled "Resonant Ultrasound Studies of Quasi-2D Na_xCoO_2." I have examined the final electronic copy of this thesis for form and content and recommend that it be accepted in partial fulfillment of the requirements for the degree of Master of Science, with a major in Materials Science and Engineering.

Veerle Keppens, Major Professor

We have read this thesis and recommend its acceptance:

Claudia Rawn, Rongying Jin

Accepted for the Council:
Carolyn R. Hodges

Vice Provost and Dean of the Graduate School

(Original signatures are on file with official student records.)

To the Graduate Council:

I am submitting herewith a thesis written by Timothy Allen Cagle entitled "Resonant Ultrasound Studies of Quasi-2D Na_xCoO_2" I have examined the final electronic copy of this thesis for form and content and recommend that it be accepted in partial fulfillment of the requirements for the degree of Master of Science, with a major in Materials Science and Engineering.

Veerle Keppens, Major Professor

We have read this thesis
and recommend its acceptance:

Claudia Rawn

Rongying Jin

Accepted for the Council:

Carolyn R. Hodges
Vice Provost and Dean of the Graduate School

(Original signatures are on file with official student records.)

Resonant Ultrasound Studies of Quasi-2D Na_xCoO_2

A Thesis
Presented for the
Master of Science
Degree
The University of Tennessee, Knoxville

Timothy Allen Cagle
December 2008

ACKNOWLEDGEMENTS

I would like to acknowledge and extend my gratitude to the following persons who have made the completion of this thesis possible:

Dr. Keppens first and foremost for her ample support and boundless patience along the way.

Dr. Rongying Jin, for sharing her talents culminating in high quality samples for study.

Dr. Claudia Rawn for her time and suggestions.

Labmates Zhiying Zhang, Yanbing Luan, Michael Koehler, Girish Upreti, David McCarthy, and Lindsay VanBebber.

Previous and current members of the Pre-Collegiate Research Scholar Program Aaron Hall and Michael Hansen.

Funding was provided by the University of Tennessee Science Alliance.

ABSTRACT

Sodium cobaltate possesses all the important traits needed in a material for potential thermoelectric applications yet it shows little regard for the traditional physics of thermoelectrics. As existing theories regarding the phenomenon in Na_xCoO_2 are incomplete, we have set out to elucidate some of the issues by looking into the elastic response of the system. To this effect, we have employed Resonant Ultrasound Spectroscopy to obtain the elastic tensor at various temperatures. As the $Na_{0.75}CoO_2$ stoichiometry seemed to potentially offer the most rewards due to a pronounced ground state and anomalous thermopower at higher temperatures, this composition was chosen for study. Polycrystal samples and floating zone grown single crystal samples were studied in temperatures ranging from 5K to 300K and in various magnetic fields from 0T to 5T.

Elastic tensors were obtained for various samples whereas the absolute values of the moduli show insufficient agreement to be conclusive. The temperature dependence however is very consistent and displays two regions of interest (30K-60K temperature range and 250K-300K range). In both regions, the material appears to stiffen with increasing temperature before relaxing back to its lower initial state. Anomalous activities at these temperatures have not been observed by most existing studies, thus have not been the subject of much discussion to date. As neither our data nor that of thermal conductivity measurements has displayed any signs of the 22K low temperature transition observed by magnetic and electronic transport measurements, it is our belief that the transition into the low temperature ground state is characterized by a rather weak coupling between phonons and the charge carriers that drive the transition. The natures of the high and low temperature anomalies are currently unclear.

TABLE OF CONTENTS

LIST OF TABLES

LIST OF FIGURES

CHAPTER 1: INTRODUCTION

Sodium Cobaltate has been shown to be a good representative material for a number of unique and sought after physical properties. With low sodium concentration, this material exhibits superconductivity when intercalated with water. Superconductivity in a transition metal oxide is an exceptional phenomenon that is aggressively being researched for numerous potential applications [1].

Sodium Cobaltate also possesses all the important traits needed in a material for potential thermoelectric applications yet it shows little regard for the traditional physics of thermoelectric power. This material has high thermopower (Q), high electrical conductivity, and reduced dimensionality (quasi-2D layers) which offers a reduction in thermal conductivity. As a result, the thermoelectric figure of merit (Z_TT), which is proportional to the square of Q and the ratio of electrical and thermal conductivities, is unusually high for a so called "dirty conductor." Traditional thermoelectric properties (Q) being derived from charge-carrier diffusion or phonon drag do not appear to be the driving source for the abnormally high thermopower inherent in Na_xCoO_2 with higher sodium concentrations. The large thermoelectric power in Na_xCoO_2 is theorized to derive from spin entropy of the charge carriers [2,3,4]. The fact that the traits that make this material potentially suitable for thermoelectric applications come from new physical phenomena makes this material very important to study in regards to thermoelectric applications.

We have employed Resonant Ultrasound Spectroscopy to study elasticity in this material. Knowledge of the elastic tensor and how it changes with temperature can provide a directional understanding of the stresses and strains and could potentially serve to constrain theories regarding thermopower and superconductivity. The literature search presented in chapter two will discuss the structure of Na_xCoO_2, magnetic moment exchange interactions, the ground state for $Na_{0.75}CoO_2$, and thermopower. Chapter three will explain the principles of RUS theory. The results are given and discussed in chapter four and a summary with suggestions for future study is presented in chapter five.

CHAPTER 2: LITERATURE REVIEW

2.1 Structure and Sodium ordering

Na_xCoO_2 is a complex material with a rich electrical/magnetic phase diagram. A large part of what makes this material remarkable is the layout of its layered structure. Na_xCoO_2 consists of triangular two dimensional CoO_2 layers with sodium atoms nestled in between. The composition or x-value refers to the amount of sodium atoms present between the sheets of CoO_2, or more specifically the ratio of sodium to cobalt atoms present in the material. Sodium acts as a charge donor and effectively contributes electrons (one per sodium atom) to the cobalt ions in the CoO_2 structure. In the absence of sodium (x = 0.0), the cobalt atoms ionize in their low spin state Co^{3+} with 5 valence electrons and carries a magnetic moment (S = 1/2). For Na_xCoO_2 where x = 1.0, there is a one to one ratio of sodium and cobalt atoms. As a result, each cobalt atom accepts an electron from a sodium atom. The cobalt atoms ionize as Co^{4+} with 6 valence electrons each and lose their magnetic moments (S = 0) as the even number of magnetic moments align anti-parallel and cancel. For compositions where $0.0 < x < 1.0$, the cobalt ions take a mixed valence state Co^{+4-x}. In this light, the structure can be seen as the layering of a triangular two-dimensional arrangement of cobalt ions and their respective magnetic moments, with moment concentration (or average valence) decreasing with increasing x [5]. At the time this study began, layered triangular lattice structures had not been studied nearly to the extent by which its square lattice counterparts have. This shortage of data makes Na_xCoO_2 important to study.

The phase diagram of sodium cobaltate is quite rich as illustrated in figure 1. With increasing x, the ground state of the non-hydrated material (hydration required for superconductivity) transitions from a pauli-paramagnetic metal ($x \approx 0.30$) to a Curie-Weiss metal ($x \approx 0.70$) to a magnetically ordered state ($x > 0.75$) [6]. Separating the paramagnetic and Curie-Weiss regions is a thin insulating region (x = 0.5) brought on by strong charge ordering [6]. Within the paramagnetic region ($x \approx 0.35$) superconductivity is induced when the material is intercalated with water [7].

The sodium ion arrangement in the crystal lattice varies quite diversely with changing sodium content. This arrangement has substantial effects on CoO_2 layer compression (crystal

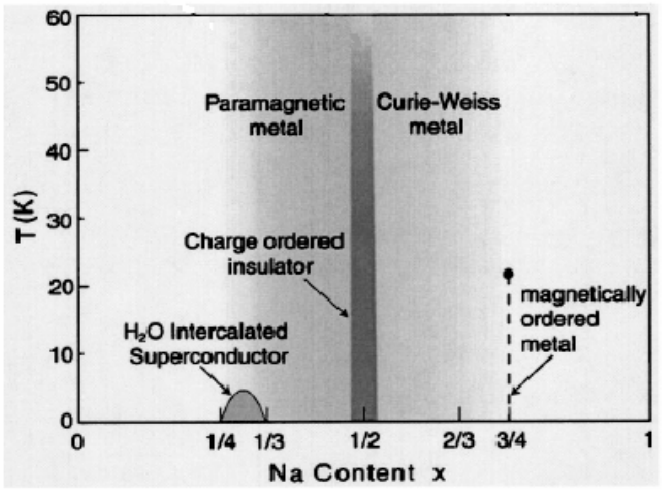

Fig. 1. Phase diagram of Na_xCoO_2 [6]

field distortion) and inter-layer distance. Though it is not always crystal clear what impact this has on the magnetic/electric properties for each region of the phase diagram, it is no doubt important and worth profiling at this point. Huang offers a structural model for the various regions of the phase diagram in relation to sodium positioning in between the CoO_2 layers and the impact this has on the CoO_6 octahedra that comprise the layers [6]. Huang postulates that the increase of the layer thickness with sodium concentration is the structural characteristic that most sensitively reflects the electronic state of Na_xCoO_2 [6]. The linear change in thickness up to around $x = 0.73$ suggests that the phase transitions are a result of continuously increasing electron count and not due to drastic structural changes (fig. 2). As the composition stretches beyond $x \sim 0.75$, CoO_2 layers exhibit a discontinuous dramatic thickening as the material changes from Curie-Weiss to a magnetically ordered metal [6].

As illustrated by Huang, the phase diagram is shown to consist of three different hexagonal structures, H1 – H3 (that are differentiated by relative sodium orientation), and an orthorhombic structure, O1, at the insulating composition ($x = 0.5$) (fig. 2). There are only two main ways, Na(1) or Na(2), in which a sodium atom can situate with respect to the CoO_6 octahedra. The distribution of the two arrangement possibilities changes with sodium content and is a defining feature for the differences between the H1, H2, and H3 structures. Na(1) ions line up directly under the center of the triangle formed by the three nearest oxygen atoms in the

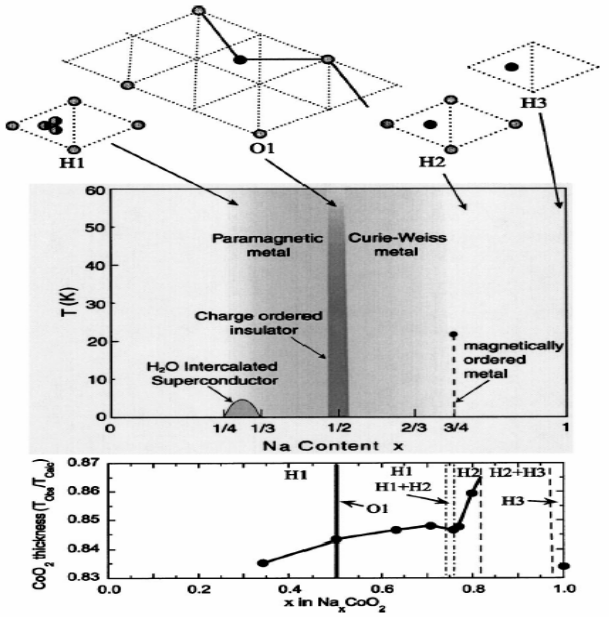

Fig. 2. Correspondence between structure and properties in Na_xCoO_2. Upper figure: schematic of the Na ion distributions in the four Na_xCoO_2 phases. Main panel: the electronic phase diagram. Lower panel: variation of the ratio of the observed CoO_2 layer thickness to the thickness of an ideal layer of octahedra. [6]

neighboring CoO_2 layer (situated directly above/below Co) (fig. 3). Due to the symmetry of the CoO_2 layers, the locations of all possible Na(1) sites form a two dimensional triangular grid that is identical to that of Co. The Na(2) sites lie in the centers of the Na(1) triangles (fig. 4) [6]. Na(1) is subject to a higher degree of coulombic repulsion (closer to Co ions) than Na(2) thus is energetically less favorable [6,8]. For the majority of the phase diagram ($0.3 < x < 0.75$), Na_xCoO_2 has the H1 hexagonal structure where the material contains both Na(1) and Na(2) sites with the ratio of Na(2) to Na(1) being greater than one due to Na(2) favoring.

The H1 region is interrupted briefly at $x = 0.5$. As the composition increases from $x = 0.3$, the Na(2):Na(1) ratio decreases and converges to unity at $x = 0.5$. At this point there is an equal population of Na(1) and Na(2) occupied sites and strong long range orthorhombic, O1, ordering is obtained possibly due to geometric symmetry and coulombic repulsion (fig. 5). The zig-zag chains of sodium ions exert a periodic coulombic potential on the charges in the CoO_2 layers which results in a periodic arrangement of charges and magnetic moments (fig. 5). The magnetic state of $Na_{0.5}CoO_2$ is substantially affected by this periodicity and is characterized as an

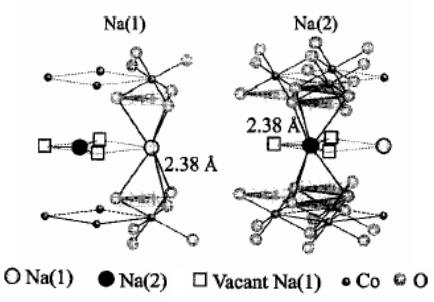

Fig. 3. The triangular prismatic NaO_6 coordination polyhedra. The Na(1) ion triangular prisms share faces with the CoO_6 octahedra. The Na(2) ion regular triangular prisms share edges with the CoO_6 octahedra. [6]

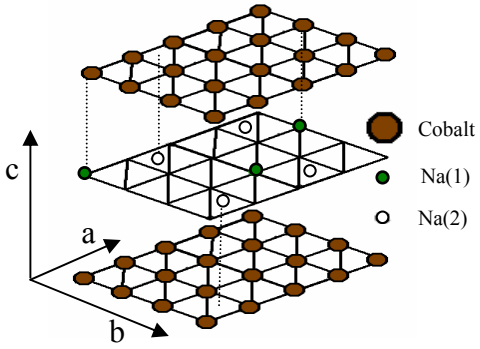

Fig. 4. Triangular arrangement of Co (charge/moment carrier) and Na(1) sites. Na(2) sites are shown in respect to the triangular Na(1) lattice.

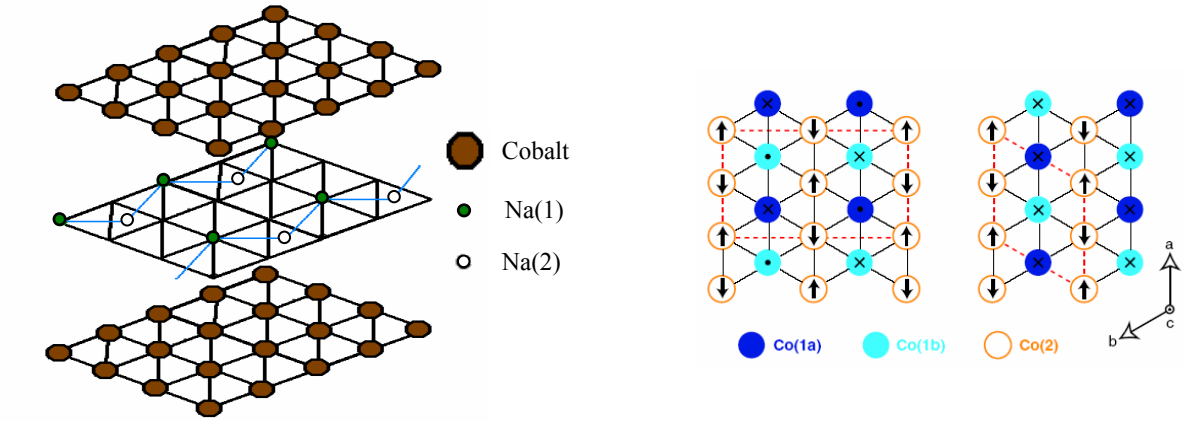

Fig. 5. $Na_{0.5}CoO_2$ periodicity. Left: Zig-zag sodium ion ordering. Right: Two possible arrangements of moments in the cobalt lattice. "Solid arrows depict in-plane moment orientation. Ordered magnetic moments on Co(1) sites point either *up* (·) or *down* (x), while moments on Co(2) sites point within the plane (arrows). Co(1) sites have either in-plane anti-ferromagnetic order (left panel) or in-plane ferromagnetic order (right panel)." [9]

itinerant anti-ferromagnet that undergoes a mysterious metal-insulator transition below ~51K [9]. Itinerant anti-ferromagnetism will be discussed in the following section.

As x increases, the strong Na superstructure quickly breaks down ("weak" long range ordering remains [8]) along with its insulating properties. The Na(1) content remains steady and all additional sodium ions occupy Na(2) vacancies. The material is once again H1 with the ratio of Na(2) to Na(1) being greater than one [6]. For x = 0.75 a relatively strong Na superstructure that is somewhat comparable to that of x = 0.5 has been observed [8]. As x increases beyond 0.75 the hexagonal structure of the material transforms from H1 to H2 where Na(1) site occupancy quickly diminishes and lower energy Na(2) sites show a sharp rise in occupancy. In the wake of disappearing higher energy Na(1) site occupancy, the CoO_6 octahedra are allowed to relax substantially and the CoO_2 layers have been observed to thicken correspondingly [6]. The octahedral relaxation reduces crystal field splitting effects on orbital energy levels and could possibly allow Hund's rule for electron orbital occupancy to play a larger role. As x progresses past $x \approx 0.82$ the structure becomes a phase mixture of H2 and H3. In this region there are H2 phases with relatively high Na(2):Na(1) ratios and H3 phases where Na(1) sites are completely unoccupied and all Na(2) sites are occupied. The H3 phases possess the stoichiometry $Na_{1.0}CoO_2$ [6]. It would appear based on arrangement and Na(2):Na(1) ratios that there is little difference between H1 and H2, but there is a subtle difference in the exact Na(2) arrangement between the two phases. In H1 the Na(2) sites are actually slightly off center (Na(2)') due to repulsions from second nearest neighbor Na(1) site occupancy [6]. In H2, Na(1) sites become increasingly vacant allowing the Na(2)' sites to recenter directly above/below the Cobalt ions in the lattice (Na(2)). At x = 1.0 the material is completely H3.

2.2 Exchange Interactions and the 0.75 Low T (<22K) Magnetic State

Interestingly, the crystal structure above the insulating composition is similar to that on the other side of the insulating state, H1 in both regions, yet the magnetic properties differ. As seen in figure 6 electrical resistivity increases with temperature indicating the metallic nature of both regions. Magnetic susceptibility, however, is markedly different above and below the insulating state. Susceptibility at x = 0.31 shows little variation with temperature but is comparable in magnitude to that of the Pauli susceptibility in conventional metals [5]. Pauli

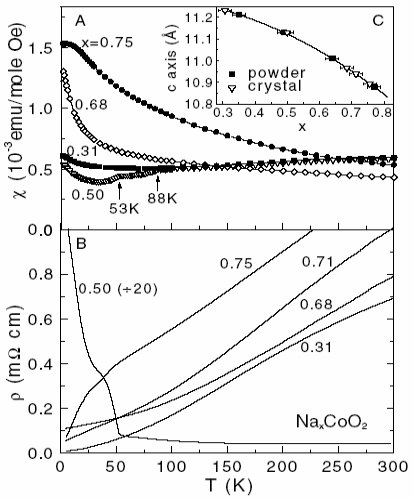

Fig. 6. Temperature dependence of resistivity and susceptibility. [5]

susceptibility is a result of weakly interacting moments where the spins are allowed to align somewhat randomly in the crystal structure despite the high concentration of moments in this region.

Above x = 0.5, the susceptibility shows a surprising Curie-Weiss temperature dependency $(T-\theta)^{-1}$ with $\theta < 0K$ [5,10]. A Curie-Weiss temperature dependency is an indication of substantial exchange interactions between the magnetic moments where the negative value of θ points toward the interactions being anti-ferromagnetic in nature for the entire region. The flattening of the susceptibility curve below 22K is an indication of magnetic saturation signifying a magnetic phase transition [5,10].

In spite of the negative θ, the exchange interactions may not be strictly anti-ferromagnetic. Using a density functional approach, Johannes suggests that there is a competition between anti-ferromagnetic (AFM) and ferromagnetic (FM) in-plane exchange interactions [11]. Previous neutron-scattering experiments attribute the 22K transition to A-type AFM ordering where in-plane FM interactions become dominant and the bulk anti-ferromagnetic nature is actually a result of oppositely aligned ferromagnetic layers [12,13,14](fig. 7). That is to say that the exchange interactions are ferromagnetic in-plane but anti-ferromagnetic between the CoO_2 layers [10,11,12,13,14] and magnon dispersion measurements show both exchange interactions to be

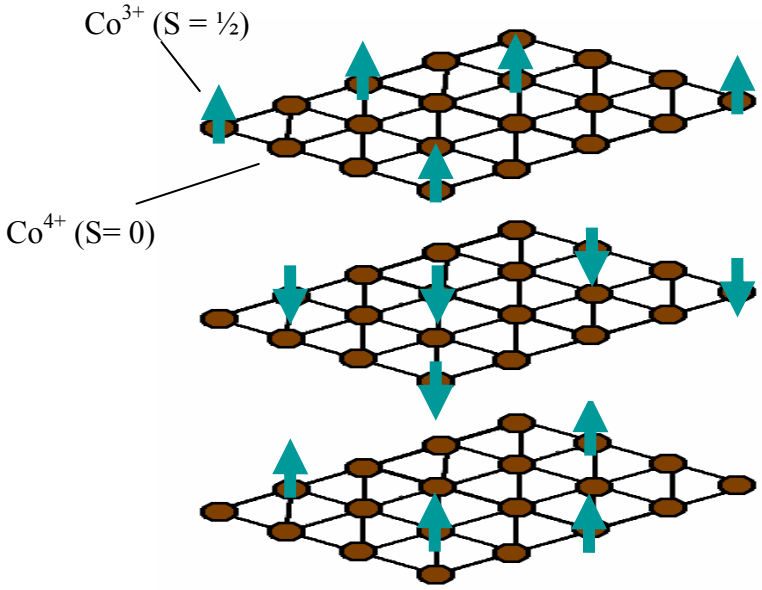

Fig. 7. A-type anti-ferromagnetic structure with in-plane ferromagnetic exchange and inter-plane anti-ferromagnetic exchange.

comparable in strength [13,14]. This is consistent with the reported metamagnetic AFM-to-FM transition in an eight Tesla magnetic field [12] where the layers whose moments are aligned anti-parallel to the external field experience spontaneous spin flipping, resulting in bulk ferromagnetic order.

A study of the low temperature (<22K) magnetic state by Sales *et al*. [15] shows that the moments are not strictly localized as could be inferred from strict A-type AFM order. Although the magnetic susceptibility data shows a clear magnetic transition at 22K that could be explained by AFM ordering with localized moments, heat capacity, resistivity, and magnetoresistance data make this explanation rather unlikely. The simple local moment scenario would call for a much larger change in heat capacity through the transition than has been found. Resistivity data make it hard to explain this discrepancy with a hypothetical undetected impurity phase [15]. The observed large increase in magnetoresisitance in cooling through the phase transition is also in disagreement with a local moment AFM transition. The shape of the heat capacity curve throughout the 22K transition, however, is exactly as would be expected from a spin density wave (SDW) transition [15]. Therefore, in this work, Sales *et al*. suggest that the observed

behavior at low T can be characterized by a spin density wave complete with large carrier mobility and itinerant exchange interactions.

Work by Sushko *et al.* [16], regarding the pressure dependency of the transition temperature, ties the localized moment and itinerant moment models together by showing that the transition occurs at higher temperatures when subjected to external pressure. This is inconsistent with the SDW model as it is understood that pressure should have detrimental effects on the stabilization of a SDW state. The work of Sushko *et al*. supports a FM in-layer/AFM inter-layer model where the moment mechanisms are both itinerant (in the AB plane) and somewhat localized (along the c-axis). Note that although the inter-layer charge mobility is suppressed ($\rho_c/\rho_{ab} \approx 600$ [15]), the strength of the exchange interactions remain comparable to that of in-layer exchanges, as was stated earlier in reference to magnon measurements[13,14].

The low temperature transition found in Na_xCoO_2 with $x = 0.75$ has been studied quite extensively and much has been learned, but a thorough understanding of the resulting magnetic state has remained elusive. As the mechanics at low temperatures are most pronounced and stable at this composition the low temperature magnetic state for $x = 0.75$ offers an opportunity to learn more about the core physics of the material. What is learned at this composition can be extended to the majority of the phase diagram as most compositions are structurally similar; this makes the physics of this region potentially important for developing a better understanding of the low temperature superconducting state. The low temperature magnetic state requires further study in order to obtain additional pieces to this complex puzzle.

2.3 Thermopower in $Na_{0.75}CoO_2$

Real world applications of thermoelectric devices are typically materialized as Peltier coolers. In such a device an electrical current induces a temperature gradient along the material parallel to that of the current. A steady flow of heat (heat current) can be established by using a heat sink to dissipate the heat build up on the hot side. This is because the material will maintain the temperature gradient by drawing heat from a material or device attached at the cool interface. In this manner, solid state refrigeration is established.

Under isothermal conditions (requiring a constant heat source and heat sink at the corresponding interfaces) the heat current is proportional to the electrical current:

$\mathbf{J}_Q = \Pi * \mathbf{j}$, *eqn*. 1

where $\mathbf{J}_Q$ is the heat current, **j** is the electrical current, and Π is the Peltier coefficient [17]. The Peltier coefficient (Π) and thermopower (Q) are related by the Kelvin relation:

$\Pi = T * Q$, *eqn*. 2

where T is temperature. From equations 2 and 3 thermopower (Q) is shown to be:

$Q = (\mathbf{J}_Q/\mathbf{j})T^{-1} = \Pi * T^{-1}$. *eqn*. 3

As the changes in heat đ**Q** and entropy d**S** are thermodynamically related via đ**Q** = T*d**S**, the corresponding fluxes of these quantities are related by $\mathbf{J}_Q = T * \mathbf{J}_S$. Equation 3 can then be rewritten as:

$\mathbf{Q} = \mathbf{J}_S/\mathbf{j}$, *eqn*. 4

which shows thermopower to be the enhanced by the entropy current (flux) [17].

In a conventional metal the entropy current is dominated by charge and phonon entropy components where thermopower (Q) is mostly unaffected by external magnetic fields. Wang *et al*. [4] have studied thermopower in Na_xCoO_2 as a function of magnetic field and have shown that it becomes completely suppressed when subject to large in-plane fields. In this light it was concluded that a large spin entropy component is responsible for the abnormally large thermopower in Na_xCoO_2. Spin entropy, typically being a result of geometric moment alignment frustrations, is rather easy to locate on the moment carrying Co lattice. As the Co ions take a triangular arrangement, there is no possible way that three magnetic moments on any given Co triangle can orient such that anti-ferromagnetic order will be established between all three moments (fig. 8). This inability to reach a low energy state induces degenerate states and subsequently magnetic moment degrees of freedom (entropy).

In addition of geometric concerns, the moment carrying charges are also subject to the coulombic potential imparted by the Na^+ inter-layer ions and rather small changes in sodium content or disorder have been known to produce striking changes in the magnetic and thermoelectric properties. The previously discussed insulating composition where x = 0.5 serves as an excellent example as rather small changes in sodium content (x) change the material from a good metal (x near but not equal to 0.5) to a strong insulator (x = 0.5). Even with fixed Na concentration the electronic structure can change depending on how the Na orders between the Co layers. As these subtle structural changes will be reflected in the elastic behavior, a study of

the elastic response of this material will lead to a better understanding of the thermoelectric properties. To this end we have employed Resonant Ultrasound Spectroscopy to acoustically study elasticity in Na_xCoO_2 as a function of both temperature and magnetic field in attempt to gain insight into the thermoelectric properties of the material.

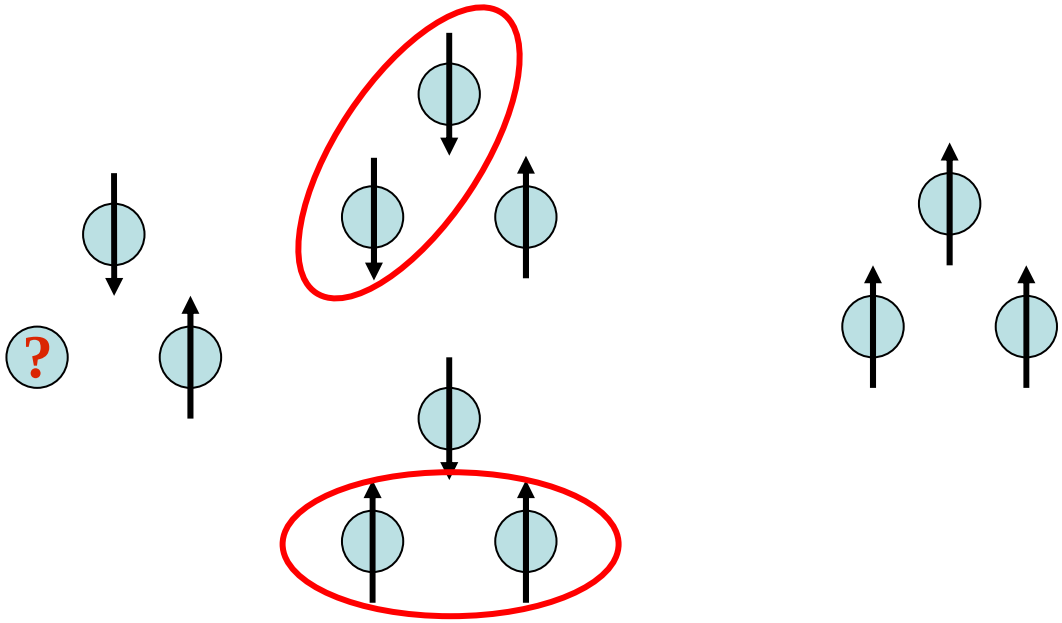

Fig. 8. Magnetic moment orientation in a triangular lattice. Left: Ambiguity and subsequent geometric frustration with anti-ferromagnetic exchange interactions. Right: Absence of geometric frustration when ferromagnetic interactions are observed.

CHAPTER 3: EXPERIMENTAL DETAILS

3.1 Resonant Ultrasound Spectroscopy

Resonant Ultrasound Spectroscopy (RUS) is a unique and sophisticated non-destructive technique for measuring the elastic tensor of a material. This approach permits the use of small, millimeter sized materials and allows the user to obtain the entire elastic tensor in one measurement. RUS has the highest accuracy of any routine modulus measurement method [18] and has successfully been used at temperatures as high as 1800K [19] and as low as 296mK [20].

Converse to the Pulse Echo method, RUS is simple to implement in the lab but complex to analyze in the office. Data is easily acquired in one measurement requiring the sample to be prepared only once. Data analysis however relies on rather complex algorithms and theories. With the proper software package, ample care taken in the lab, and a little luck, data analysis is immensely simplified, making the entire process from beginning to end comparatively simple.

The fundamental principle behind RUS is used routinely in daily life. It is common practice to test the freshness of a watermelon by tapping on the rind and listening to the sound it makes. The deeper and thicker the sound, the fresher the fruit is. The freshness test is a practice in communication between the user and the material. In the above examples, the experimenter applied an external physical stimulus and the material produced a mechanical acoustic response. Resonant Ultrasound Spectroscopy employs the very same principles of communication, albeit much more constrained and elaborate. The external stimulus (induced pressure at precise frequencies) is more controlled; and the response is more defined (locations of resonant frequencies - modes). The materials under investigation are also much more complex than the above-mentioned watermelon with rigid shape constraints and well-defined crystallographic structure. The payoffs make the added effort more than worthwhile as a lot of information can be obtained in the process such as elastic constants, insight into the internal friction losses, and presence of phase transitions.

The following sections will discuss the details of Resonant Ultrasound Spectroscopy. Section 3.1.1 will describe the experimental setup while section 3.1.2 will discuss the various aspects of data processing, or how the elastic tensor is obtained from “raw frequencies.”

3.1.1 RUS - Apparatus

As was previously stated, one of the fundamental principles behind RUS is to drive the material at well defined frequencies and to extract precise locations for the resonant frequencies. The physical muscles in the system are two piezo-electric transducers. The first transducer converts the applied electrical signal to a mechanical stress at the surface of the material. The other transducer is responsible for picking up the physical response of the material and converting it back into an electrical signal for data acquisition and subsequent analysis (fig. 9). A program written in Labview was designed to drive a function generator to sweep over a wide frequency range while the output from the sample probe is sent through a series of amplifiers back to the computer (fig. 10). It is stressed that the action through the sample is purely mechanical. The transducer faces, serving as points of contact with the sample, are electrically grounded. There is no direct electrical transmission through the sample probe.

There is a complication as the signal is weak compared to the noise in the system. To circumvent this issue a "lock-in" amplifier was used to compare the raw output signal from the probe to that of the input signal coming from the function generator (fig. 10). All elements of the output signal that did not match the driving signal in both frequency and relative phase were eliminated.

To get an understanding of how the elasticity of the material changes with temperature and in the presence of high magnetic fields, scans have to be repeated in these conditions. To serve this purpose, the sample probe is inserted into a Quantum Design Physical Property Measurement System that allows measurements as a function of temperature between 2 K and 400 K, and in magnetic fields up to 9T.

3.1.2 RUS Theory – Data Processing

As was stated at the beginning of the chapter, the data analysis aspect of RUS is responsible for the lion's share of the complexity. Knowing the frequencies of resonance is nice, but how do they translate into an elastic tensor? The answer is rather convoluted and requires a bit of discussion on a number of topics. We can start by overcomplicating the equation of motion for a simple harmonic oscillator with Lagrangian mathematics. A good illustrative example is a simple one-dimensional spring-mass system (fig. 11). The Lagrangian for a single-element discrete system is:

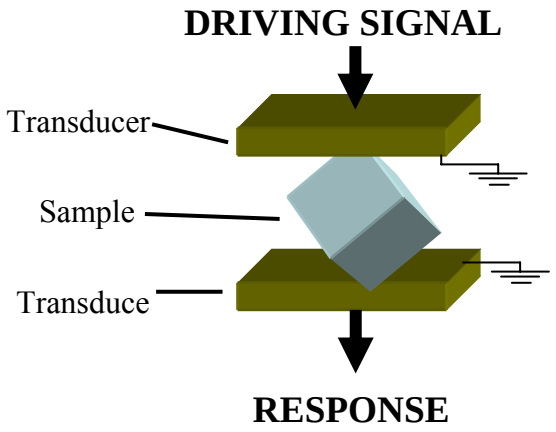

Fig. 9. Sample probe components. Driving signal mechanically stimulates sample through piezo-action of the top transducer. Conversely the bottom transducer generates an electrical response.

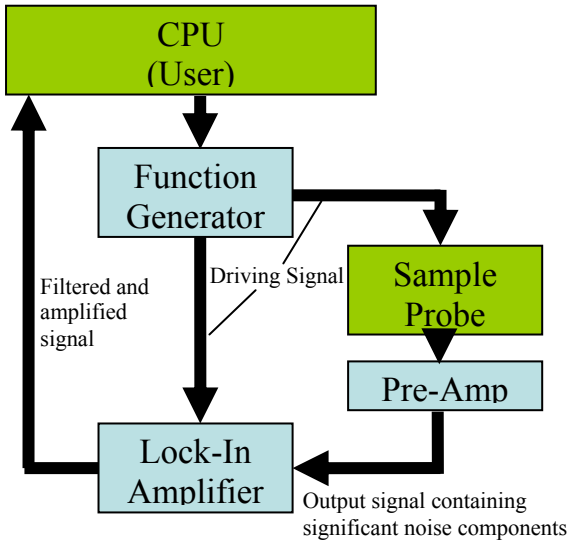

Fig. 10. RUS Flow Chart

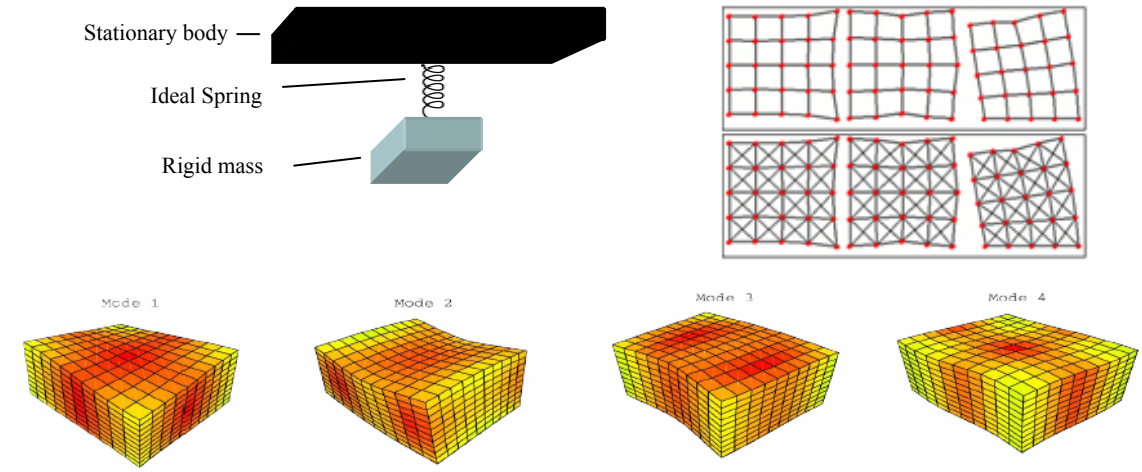

Fig. 11. Single and multi-bodied harmonic systems in various dimensions. Top left: Simple harmonic oscillator. Top right: Two dimensional multi-bodied spring-mass system [21]. Bottom: Various actual modes inherent to 3-D parallelepiped materials, as studied in lab [22].

$$L = T - V. \qquad \textit{eqn.}\ 5$$

Where T = Kinetic Energy = ½ mv^2 and V = Potential Energy = ½ kx^2. Therefore,

$$L = \frac{1}{2} m \dot{x}^2 - \frac{1}{2} k x^2 . \qquad \textit{eqn.}\ 6$$

Hamilton's Principle of Least Action states that the true trajectory is that function which minimizes the action of the system. Lagrangian mathematics allows for the action minimization of simple systems by applying the Euler-Lagrange formula (*eqn*. 7) to the Lagrangian (*eqn.* 6) [23]

$$\frac{\partial L}{\partial q_i} - \frac{d}{dt}\left(\frac{\partial L}{\partial \dot{q}_i} \right) = 0 , \qquad \textit{eqn.}\ 7$$

where q_i is the "generalized" coordinate. In this scenario x is substituted for q yielding:

$$\frac{\partial L}{\partial x} - \frac{d}{dt}\left(\frac{\partial L}{\partial \dot{x}} \right) = 0 . \qquad \textit{eqn.}\ 8$$

Applying equation 8 to the Lagrangian (*eqn* 6) while treating *x* and $\dot{x}$ as independent variables yields the equation of motion for the system. $-kx = m\ddot{x} = ma$. Via Newton's law F=ma, we now have derived Hooke's law of elasticity in a rather roundabout manner. Indeed it would have been simpler to use Newton's law to begin with as is typical of most simple systems. The strength of Lagrangian's formulation shows up when we consider complex, multi-bodied, multidimensional systems (fig. 11). In our case we are not focused on the motion of the sample as a single rigid body, rather an immensely complex system comprised of seemingly infinite constituent atoms and their motions relative to one another. In such a system the Lagrangian becomes

$$L = \int_V (KE - PE) dV \qquad \textit{eqn.}\ 9$$

where

$$KE = \frac{1}{2} \sum_i \rho \omega^2 u_i^2 \qquad \textit{eqn.}\ 10$$

and

$$PE = \sum_{i,j,k,l} c_{ijkl} \frac{\partial u_i}{\partial x_j} \frac{\partial u_k}{\partial x_l} \qquad eqn.\ 11$$

[18]. Derivation of the equation of motion in this system is not quite as straight-forward as it was for the simple harmonic oscillator but the principles remain the same resulting in the eigenvalue equation

$$\omega^2 \overleftrightarrow{E}\vec{a} = \overleftrightarrow{\Gamma}\vec{a}\,. \qquad eqn.\ 12$$

With the elastic tensor being a large matrix we should not be surprised to see matrices in the equation of motion. Most of this equation is mathematical constructs with little or no physical interpretation. The true variables underlying this mess are density (E(ρ)), the elastic tensor ($\Gamma(c_{iji'j'})$), and the resonant frequencies. (See Migliori for a proper derivation [18]). The eigenvalues for this equation turn out to be the free-oscillation frequencies and the eigenvectors are physical displacements when oscillating [18].

Unfortunately equation 12 is a one way street. Calculating the frequencies from the elastic tensor is a "simple" matter that is done routinely with in-lab software. The opposite is not true. There is no direct approach to fill the elastic tensor from knowledge of the resonant frequencies. Rather unfortunate indeed as this is precisely what we aim to do as the frequencies are measured in the lab. The solution to this dilemma is iterative in nature. If we can make an educated guess as to what the values of the tensor might be, then we can calculate hypothetical resonant frequencies for comparison with those found experimentally. This allows for an adjustment of the initial guess and a new set of hypothetical frequencies for comparison. This process is repeated until the calculated and measured frequencies agree (fig. 12). At this point the elastic tensor has been determined to a large degree of confidence.

A polycrystal output file for 120K is provided by figure 13 as an example to illustrate some of the key aspects of this process. The collimated section in the upper portion of figure 13 represents the first 29 resonant frequencies for this material. The "fr" column depicts the hypothetical frequencies that were derived from the initial guesses and subsequent adjustments as previously described. The degrees to which the hypothetical and experimental ("fex" column in fig. 13) individual frequency values agree are listed in the error column "%err."

The zeroes in the seventeenth row denote a frequency that was not detected through

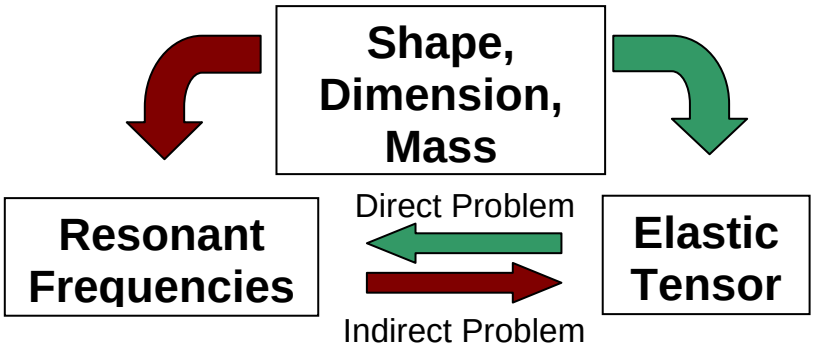

Fig. 12. Principles of RUS. The elastic constants can iteratively be determined from the density of the material, an initial guess of the constants, and the frequencies of resonance.

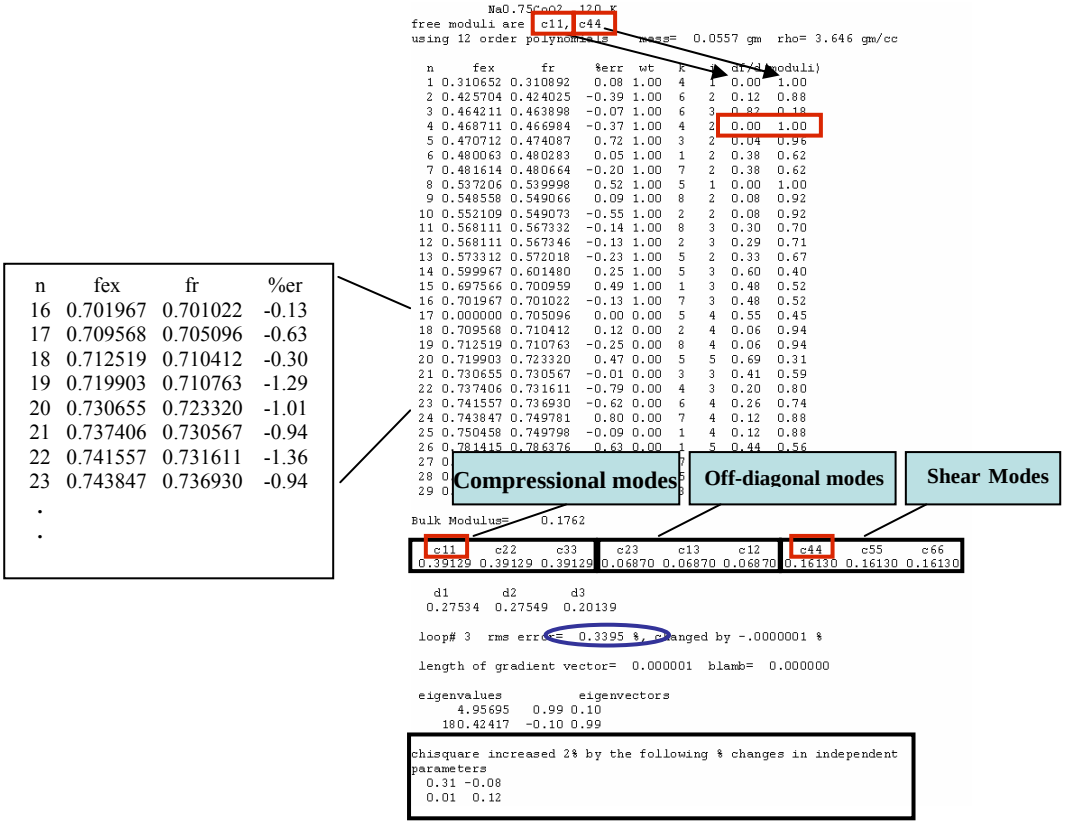

Fig. 13. $Na_{0.75}CoO_2$ polycrystal output file for data taken at 120K.

experimentation. It is not uncommon for modes to go undetected as they can be small and easily lost in the background. The zeroes were manually added to prevent mismatch in the remaining frequency comparisons. The box on the left shows this portion of the output file before the missing frequency was accounted for. The significant errors for subsequent modes were a result of comparing sequentially unmatched frequencies.

The numbers in the last two columns denote the sensitivities of the given frequency to the fitted elastic moduli (c_{11} and c_{44} for the polycrystalline example), and are normalized to unity ($df/dc_{11} + df/dc_{44} = 1.0$). The sensitivities are very important as they provide very useful information that can be utilized in many ways. Mode 4 serves as an excellent example as it is shown to be completely dependant on c_{44} and not at all on c_{11}. This heavy dependency allows us to track the change of the given constant (c_{44} in this case) under various changing conditions (temperature, pressure, etc…) without having to compute the full tensor for each data point. This is done by plotting the square of the given frequency as a function of the variant condition (the remainder of this paper will consider temperature exclusively) as the equation of motion (***eqn.*** 12) shows that the elastic constants are proportional to the squares of the frequencies. On their own, the squared frequency plots do not provide information about the absolute values of the elastic constant in question, but they are very helpful in many regards as will be seen in the following chapter.

The results are listed directly below the collimated section. The data here is a combination of values that were directly determined via the fitting routine (c_{11} and c_{44} for the polycrystal example having only 2 independent constants) and dependant values calculated from the fitted values on the basis of crystal symmetry. As the sample of figure 13 is of isotropic symmetry, the compressional modes c_{11}, c_{22}, and c_{33} are identical. The same can be said of the off-diagonal and shear modes respectively. The off-diagonal modes and bulk modulus were calculated on the basis of isotropy from c_{11} and c_{44} with the equations $off\_diag = c_{11} - 2c_{44}$ and $bulk = c_{11} - (4/3)c_{44}$.

The number of iterations required for convergence, the overall root mean square error (RMS) between the fitted and measured frequencies, and the change in RMS between the present and previous iteration can be found further down the output file. The chi square values are located at the bottom of the file and are discussed in the following chapter.

3.2 Sample Synthesis and Preparation

3.2.1 Sample Synthesis

High purity powders of Na_2CO_3 (99.997% from Alfa-AESAR) and Co_3O_4 (99.999% from Alfa-AESAR) were carefully weighed to give the desired stoichiometry of $Na_{0.75}CoO_2$. The powders were first mixed by hand to yield a homogenous gray color and then ball milled for 2 hours. The ball milled powder was loaded into a high purity (99.9%) alumina tray, inserted into a 750 °C preheated furnace, and left for 20 hours. This rapid-heat technique was found to minimize the loss of Na due to volatilization [24]. For polycrystalline samples, some of the pre-reacted powder was pressed into 1 inch diameter pellets and placed on a thin layer of the same powder in an alumina tray. The pellets were heated to 830 °C for 16 hours in pure O_2 that was slowly (≈10 cm^3/min) flowing over the tray, and then cooled to room temperature over a period of 6–8 hours. Single crystal samples were prepared from most of the remaining pre-reacted powder using a floating zone method. The powder was hydrostatically compressed in rubber bladders into 6 mm diameter by 100 mm long rods. The fragile rods were carefully removed from the bladder, placed in an alumina tray on loose powder with the same composition, and heated at 830 °C for 16 hours in flowing oxygen. The polycrystalline rods were used in an NEC SCM15-HD arc image furnace to prepare single crystals of $Na_{0.75}CoO_2$ and $Na_{0.77}CoO_2$ via the floating zone method with typical growth rates of 2–5 mm/h.

3.2.2 Sample Preparation

For accurate elastic constant calculations, the fitting routine requires a well shapen material with tight geometric tolerances as the algorithms employed are based on a well defined geometric shape. Strict geometry is also important for density calculations and avoiding degeneracy and overlap of the frequencies of resonance. This section will explore the method of preparing rectangular parallelepiped samples (that exceed the stringent tolerances) from single crystalline rods and polycrystalline pellets.

To acquire a good fit, the overall geometric errors combined can be no worse than one part in 10^3 [18]. The faces should be smooth and free of pits and cracks. Alignment of the faces with the crystal structure is somewhat lenient. A 1° misalignment produces a tolerable error of a

few parts in 10^4, allowing an overall misalignment of a few degrees. Perfection in the parallelism and perpendicularity of the faces is much less forgiving and demands perfection on the order of 1μm/mm as such errors couple to some modes but not to others [18].

The process began by creating an initial good surface on the material around which the alignment of the rest of the sample can be centered. The initial cut is a nontrivial matter when considering anisotropic materials. As was previously stated, RUS requires alignment of the sample faces with the crystallographic microstructure. This is a non-factor for the isotropic polycrystalline samples. The polycrystalline pellets were cut into manageable sizes with a diamond saw. Because there are no alignment concerns with polycrystalline samples, any of these cuts could be used as the initial surface for the polishing routine. This is not the case for the anisotropic single crystalline samples. The symmetry in this material is hexagonal with elastic isotropy only in the AB plane (i.e. plane perpendicular to hexagonal c-axis). This dictates the necessity of orientation with respect to the c axis. By polishing the sample such that two opposing faces are in the AB planes, the sample will have the c axis perpendicular to these faces. Fortunately the layered structure of Na_xCoO_2 provides a way to locate the AB plane that does not necessitate the use of X-ray analysis. This stems from the ease with which the AB planes tend to shear apart under direct pressure. It is not a "needle in the haystack" search either since the planes lie in the direction of rod growth, a well determined direction (fig. 14). The rod was initially cut with a diamond saw into smaller discs. With the AB plane projecting along the height of the discs, it was a simple matter of rotating the disc and applying pressure with a very sharp scalpel at various locations along the edge of the disc until the sample sheared apart. Careful scrutiny under an optical microscope revealed regions of good shearing as they shined quite lustrously. The low quality regions were then worked away with the scalpel such that only the high quality surface protruded. This surface served as the basis by which subsequent polishing was made.

Once the initial surface had been adequately obtained the sample was ready to be polished with shims, a magnet, and some sandpaper. The sample was placed on a flat magnetic surface with the pre-cut surface face down on the magnet. The sample was held firmly by a set of four nearly identical shims in a star formation (fig. 15). Using fine sandpaper mounted on a flat microscope slide the top face was polished down to the surface of the shims. This side was now

precisely flat and – depending on the accuracy of the initial cut – well aligned with the AB plane of the hexagonal crystal structure. The sample was flipped and the precut face was polished to the dimension of a smaller set of shims. At this point the sample had two very flat very parallel faces by which the remaining four sides were subsequently polished. This process molded the sample into a rectangular parallelepiped shape with flat smooth surfaces, with high degrees of parallelism and perpendicularity, and with good alignment to the crystal structure.

As a final note, it is desirable that the final lengths of the sample differ, as geometric symmetry will produce degenerate resonances. It is critically important in RUS not to miss any resonances or a fit can never be produced. Degenerate resonances will be indistinguishable making it impossible to determine the number of nodes at a given frequency. This constraint is easily satisfied by using sets of shims that differ by height.

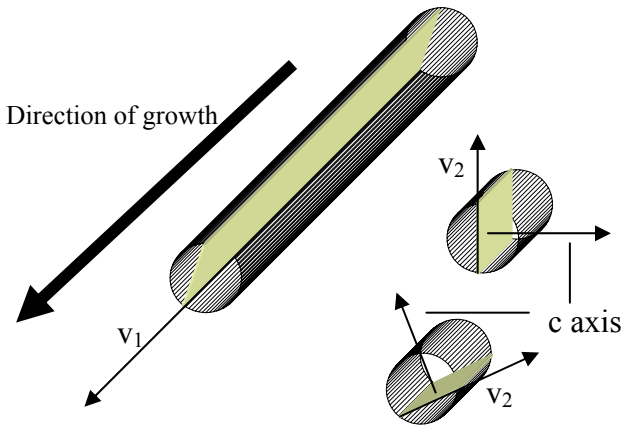

Fig. 14. Illustration of orientation and growth direction. Of the two vectors that define the AB plane, one is determined by the direction of growth (v_1). The second is found by cleaving the sample with a scalpel (v_2). The c-axis is orthogonal to these two vectors.

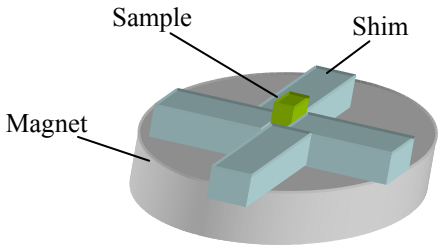

Fig. 15. Polishing Apparatus

CHAPTER 4: RESULTS AND DISCUSSION

The results of our study are listed and discussed in this chapter. In total, thirteen samples have been studied with various magnetic fields, mounting positions, and other varying conditions. Thirty-one total runs were made in the PPMS equaling well over six-hundred hours of data acquisition alone. For clarification purposes, the data that will subsequently be discussed in this chapter are summarized in tables one and two.

The majority of the runs did not produce data of sufficient quality for analysis and are not listed. RUS requires the accurate determination of the frequencies of resonance and cannot accurately calculate the elastic tensor where modes are missing. As was discussed in chapter three, a skilled user can identify missing modes from the output file, but this can only be realistically done if the data is of sufficient quality where the resonant peaks are mostly clean and missing modes are few. Figure 16 has been provided to illustrate some of the difficulties associated with low quality data. The difference is not hard to observe. High quality data produces very well shapen narrow peaks with a high signal to background ratio. This enables accurate determination of the frequencies of resonance and minimizes the likelihood of missing too many modes. The low quality data in this example has too many ambiguities making precise frequencies difficult to determine and increases the probability of missing numerous modes. As figure 16 is just an example, it is by no means an all inclusive depiction of what can be expected of the frequency spectrum. The quality of data comes in varying degrees and individual frequency spectrums have various difficulties associated with them (split peaks, low signal to noise, etc…).

We believe that the low yield of quality data was a result of moisture contamination as this material is highly sensitive to water. Although ample preventative care was taken, prolonged humidity exposure during sample preparation was unavoidable. Water exposure for some samples was also a result of a temporary malfunction in the PPMS that caused a slow leak which in turn allowed moisture into the sample chamber.

Table 1. Summary of $Na_{0.75}CoO_2$ polycrystal data sets discussed in this chapter.

Sample	Weight (gm)	Field (Tesla)	Fit
1	0.0181	0	yes
2	0.0552	0	yes
3a	0.0288	0	no
3b	0.0288	5	no

Table 2. Summary of Na_xCoO_2 single crystal data sets discussed in this chapter.

Sample	x	Weight (gm)	Field (Tesla)	Fit
1a	0.75	0.011	0	yes
1b	0.75	0.011	5	yes
2	0.75	0.0156	0	yes
3	0.77	0.0345	5	no

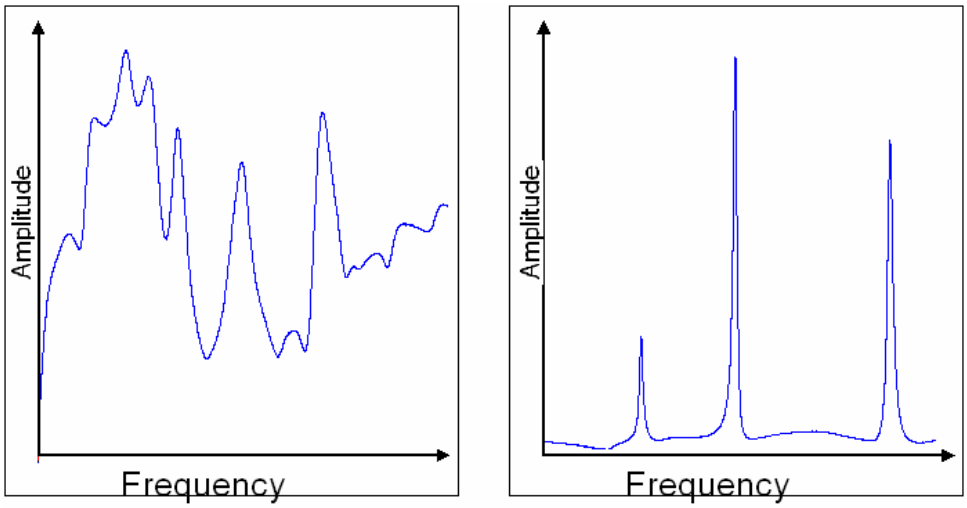

Fig. 16. Representative frequency spectrums (bad vs. ideal)

4.1 Polycrystalline Samples (x = 0.75)

Three polycrystalline samples were prepared for study. Of these, two samples produced frequency spectrums of sufficient quality to determine the independent elastic constants (c_{11} and c_{44}) with the fitting routine. The longitudinal modulus (c_{11}) and the shear modulus (c_{44}) were used to calculate the bulk modulus, Poisson's ratio, Lame's constant, and Young's modulus. Unfortunately, the calculated independent elastic moduli were not in sufficient agreement to conclude with confidence that they had been accurately determined. Using the 120K fit as an example (fig. 13) the difference in c_{11} was approximately 27% and 17% for c_{44}. As the remaining constants were calculated from c_{11} and c_{44} they also display substantial differences. The results are summarized in table 3.

For RUS, useful information can be obtained even in the absence of a high quality fit (a well determined tensor). As discussed in the previous chapter, the elastic constants are proportional to the square of the frequencies of resonance. With this relation, temperature dependencies of the elastic moduli can be obtained by plotting squared frequencies against temperature and are shown in figure 17 for the three prepared samples. Any deviation from "normal" behavior (fig. 18) can be interpreted as anomalous behavior and is often indicative of a phase transition. An elastic "hump" is apparent in all three samples between 30K and 60K. As this temperature range is above the 22K phase transition that was discussed in section 2.2, the latter is most likely not related to the observed elastic "hump".

Table 3. Polycrystal elastic constants (10^{11}Pa) at 120K. Similar results were found at all temperatures.

	Sample 1	**Sample 2**	**difference**
Longitudinal	0.517	0.39129	27.68%
Shear	0.1924	0.1613	17.59%
Bulk	0.26	0.1762	38.42%
Poisson's	0.203209	0.149297	30.59%
Lame's	0.131733	0.068667	62.94%
Young's	0.462995	0.370763	22.12%

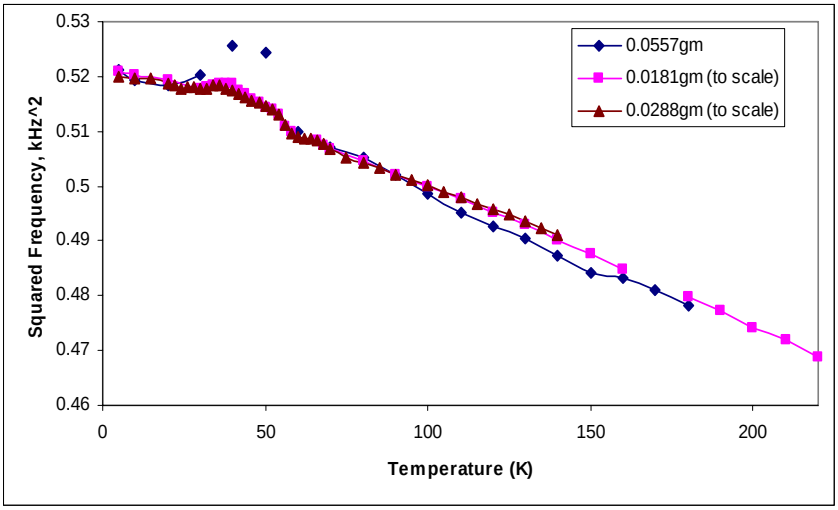

Fig. 17. Scaled temperature dependency of squared resonant frequencies for the three polycrystalline samples (x=0.75).

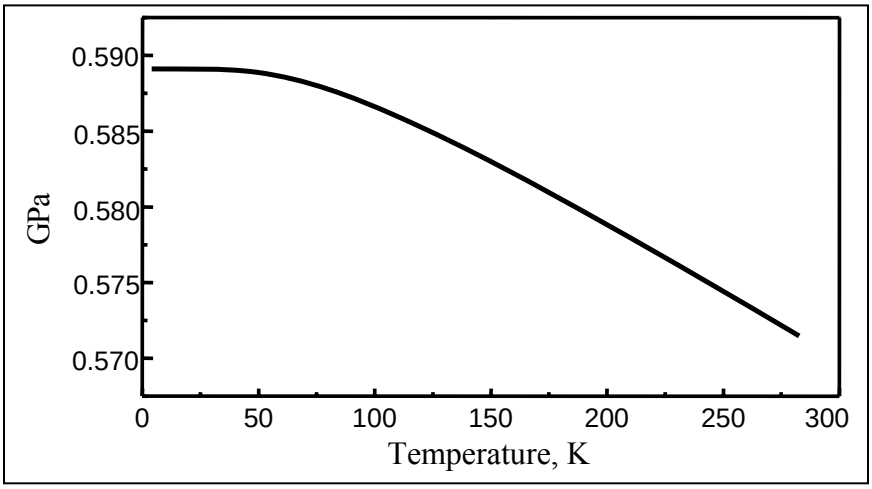

Fig. 18. Example of "normal" elastic behavior vs. temperature. Material stiffens to a maximum as temperature drops without any deviations or anomalous behavior.

It has been observed in the lab that the presence of an external magnetic field sometimes has positive effects on the quality of the frequency spectrum. With this in mind, RUS measurements were made on another polycrystalline sample (sample 3) from 5K to 300K in a 5 Tesla field. Though an elastic fit could not be obtained, the experiment did produce adequately shaped resonant frequencies at higher temperatures where the zero field data appeared "washed out." The resulting temperature dependencies are shown in figure 19. In addition to the previously observed low temperature hump (fig. 20), an additional anomaly is observed at higher temperatures (215K – 250K). It would seem appropriate at this time to delve into the effects of field on the material. As will be seen in the figures of the subsequent section, however, the external magnetic field does not consistently produce positive effects for additional temperatures.

4.2 Single Crystal Samples (x = 0.77, 0.75)

Single crystal samples of stoichiometric $Na_{0.75}CoO_2$ and $Na_{0.77}CoO_2$ were studied in temperatures ranging from five kelvin to three-hundred kelvin. $Na_{0.75}CoO_2$ sample 1 produced fits both in zero field and in an external five tesla magnetic field. The temperature dependence for the calculated shear modes c_{44} and c_{66} are plotted in figures 21 and 22. The low temperature and high temperature anomalies that were found in the polycrystalline samples are also observed in the single crystals but the high temperature "hump" moved to higher temperatures (250K-300K)

It is important when calculating the elastic tensor at various temperatures to keep the fitting conditions as identical as possible. If thirty peaks were used for the 120K fit, for example, then the same thirty peaks should be used for all temperatures to avoid extra scatter in the resulting data. Such scatter can show up in the temperature plots and indicate anomalous behavior where none actually exists. As a result figures 21 and 22 have many gaps at temperatures where various peaks disappeared, split, or otherwise prevented accurate identification.

Fortunately RUS provides the means by which to fill these gaps as well as smooth the existing data of the unavoidable scatter associated with the numerous temperature fits [18]. As discussed in the previous chapter, the mode sensitivity (df/d(moduli)) columns in figure 23 indicate the dependency of a particular frequency on the independent constants (five here for

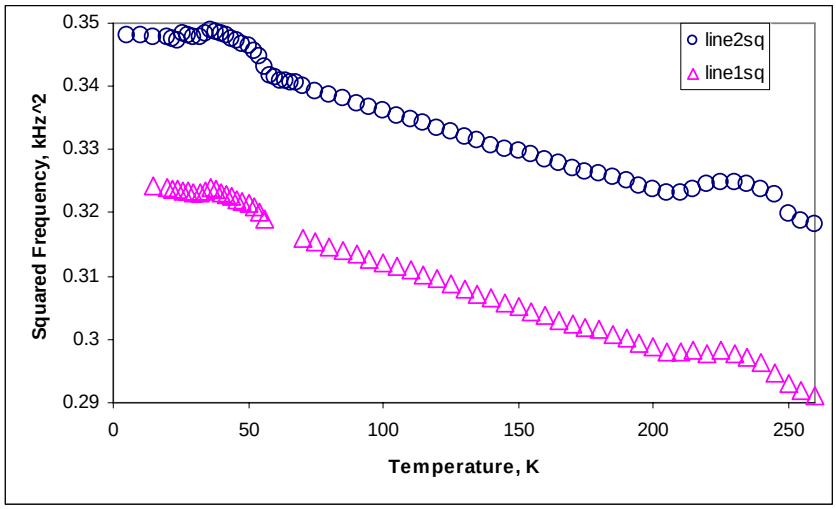

Fig. 19. Squared resonant frequencies vs. temperature for a polycrystal sample (sample 3) in a 5 T field(x=0.75). Two representative frequencies are shown.

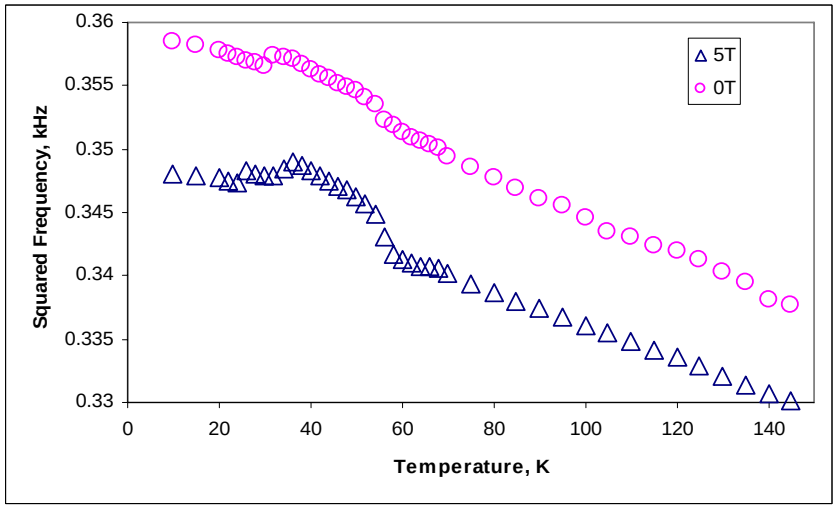

Fig. 20. Polycrystalline elastic trends for sample 3 in zero and five tesla fields (x=0.75). Zoomed in on low temperature region for comparison.

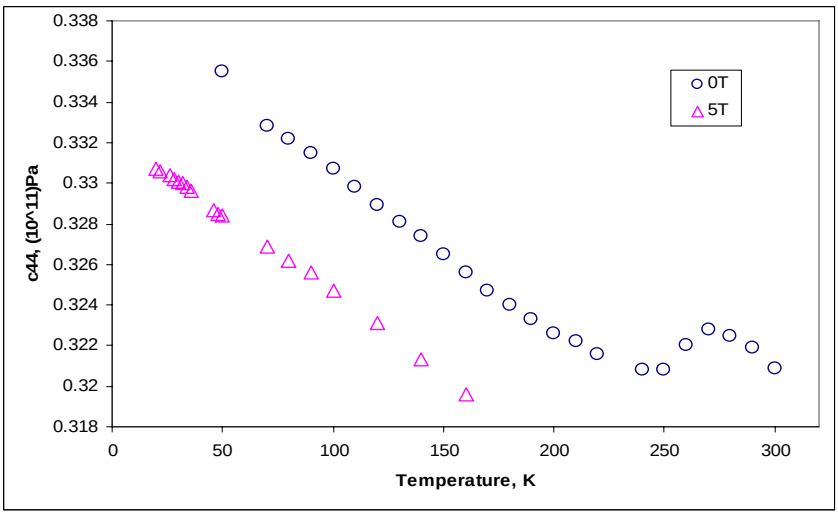

Fig. 21. Shear mode c_{44} vs. temperature for single crystal sample 1.

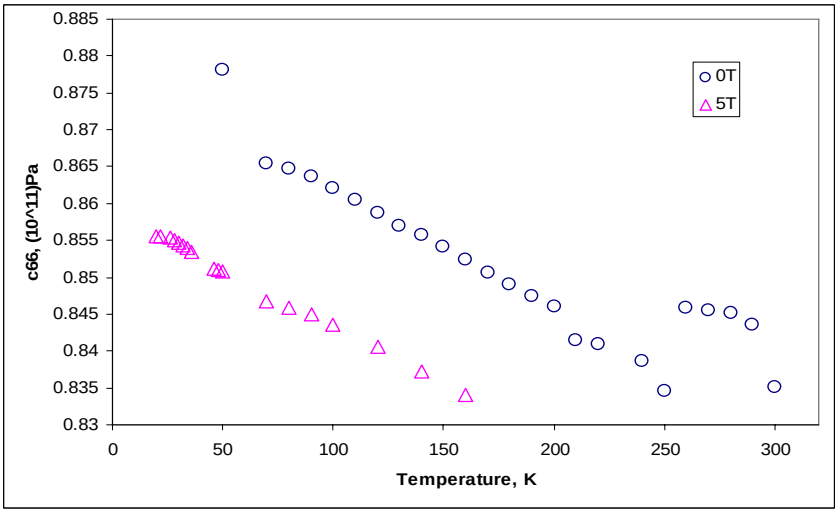

Fig. 22. Shear mode c_{66} vs. temperature for single crystal sample 1.

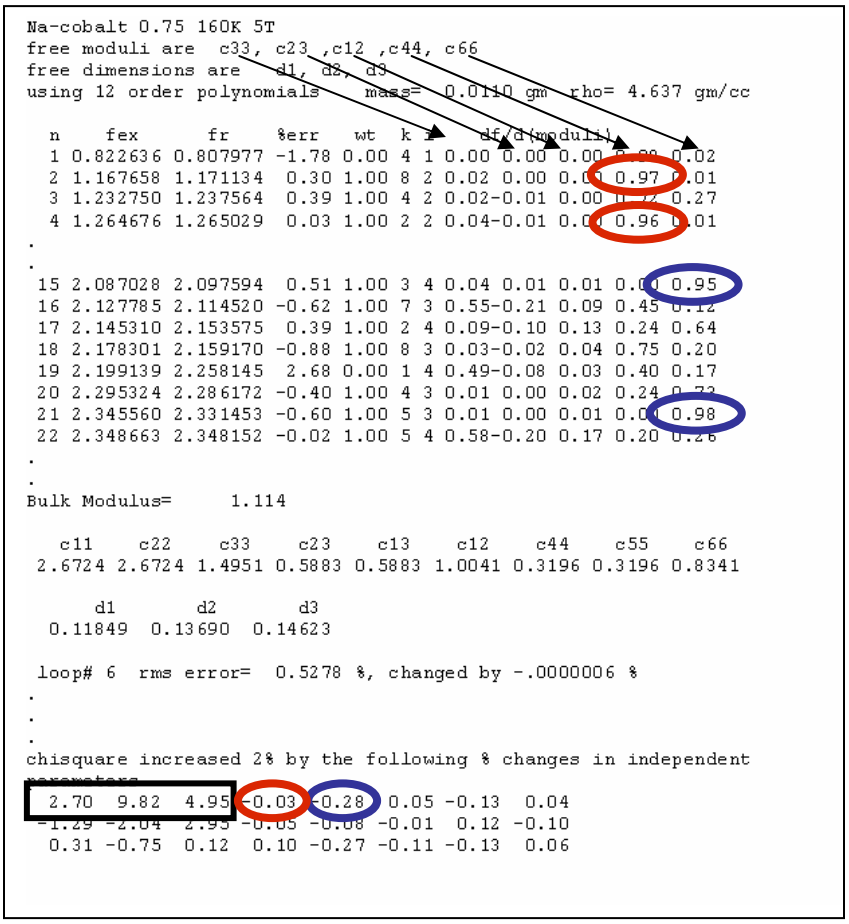

Fig. 23. Fitting routine output file example (sample 1 in a 5 tesla field). Red and blue ovals indicate c_{44} and c_{66} modal sensitivity and chi^2 values respectively. Black square highlights inaccuracy for c_{33}, c_{23}, and c_{12}.

hexagonal structure). Modes two and four are almost exclusively c_{44} dependant where modes fifteen and twenty-one are heavily c_{66}. As a result of these heavy dependencies, squared frequency plots of these modes accurately depict the temperature dependencies of c_{44} and c_{66} respectively. The squared frequency data can then be normalized with calculated values at a given temperature to obtain accurate data where the temperature gaps have been filled (figures 24 and 25).

There are five independent elastic constants for hexagonal crystal structures yet only two (c_{44} and c_{66}) have been presented and discussed. A look at the chi-square section in figure 23 offers an explanation. For each calculated constant, its chi-square value indicates the amount of "slop" allowed in the value of the constant before the overall error changes substantially. A low number is preferential as it reduces ambiguity. As an example, in figure 23 c_{12} was determined to be $1.0041(10^{11})$Pa with a chi-square value of 4.95%. The high chi-square value stretches the possible values for c_{12} to be between $1.05(10^{11})$Pa and $0.95(10^{11})$Pa. This is detrimental to temperature plots as each data point has a very large error bar. This has the effect of generating substantial scatter in the plot that completely masks its much more subtle features. Due to high chi-square values, c_{33}, c_{23}, and c_{12} were rejected for unreliability.

The average difference for c_{44} between the zero and five tesla data was 1.68%, and 1.96% for c_{66}. Similar to polycrystalline field data (fig. 20), the presence of an external field seemed to have the effect of softening the material across all temperatures. It would be interesting to link this softening to the suppression of thermopower in magnetic fields. To establish such a connection it would be helpful to first show a relationship between elasticity and thermopower (Q). If such a connection existed, one would expect to see anomalous behavior in Q at the same temperatures where we have shown such behavior in elasticity. The Q vs. temperature plot provided by Wang *et al.* [4] (fig. 26) however does not display any signs of such activity. The low temperature inflection in Q appears to be more consistent with the T = 22K transition and nothing is observed at higher temperatures. It seems a bit preemptive to rule out the possibility of any such correlation. A more in depth study of field softening at various fields would be required. It would most certainly be interesting to study elasticity in fields near the 8T value where complete suppression of thermopower has been observed.

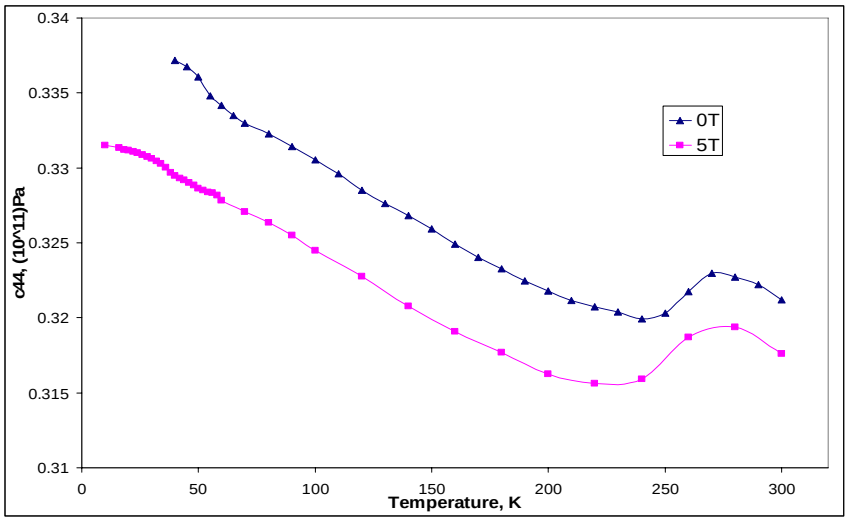

Fig. 24. Sample 1 shear mode c_{44} normalized with frequencies two and four.

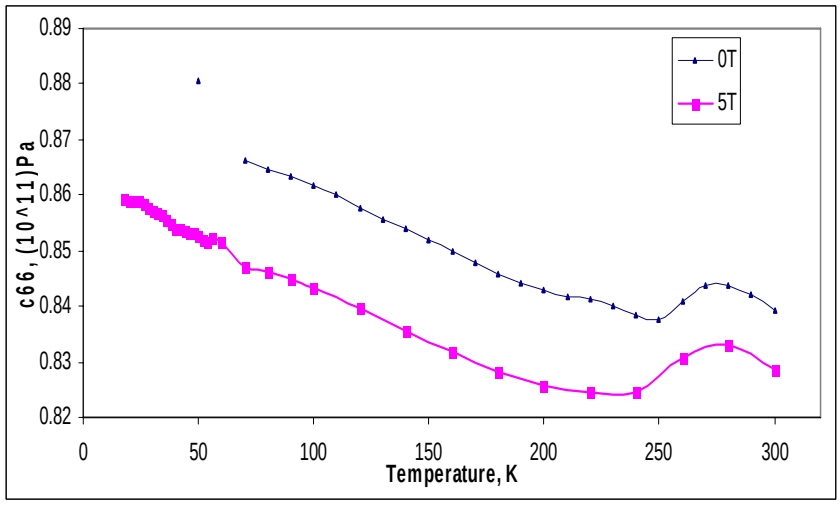

Fig. 25. Sample 1 shear mode c_{66} normalized with frequencies fifteen and twenty-one.

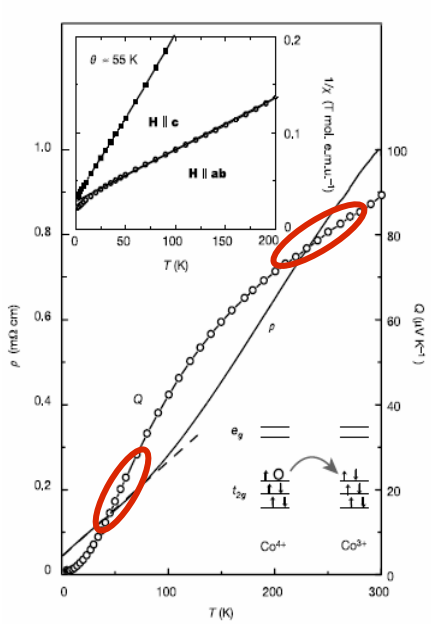

Fig. 26. Thermopower (Q – open circles) as a function of temperature for single crystal $Na_{0.75}CoO_2$. The red ovals point out regions where elastic anomalies have been observed. [4]

$Na_{0.75}CoO_2$ sample 2 was studied with various mounting positions and magnetic fields as part of a large data acquisition regiment in the hope of finding at least a couple batches of good data. Unfortunately, a noticeable amount of moisture in the PPMS sample chamber was detected when the sample was eventually removed after a long stint without removal. Careful analysis of degradation in the frequency spectrums for each data set led us to the conclusion that the leak was slow enough to leave the data from the first couple runs relatively unspoiled.

With no magnetic field applied, an elastic tensor was calculated when this sample was flat mounted with the sample faces making contact with the transducers. Also in the absence of a magnetic field, a fit was produced for the same sample when mounted with opposing edges making contact. As this work was performed recently, a full analysis of temperature dependant behavior has not been completed for this sample. The remaining scans with this sample (as well as those not mentioned for sample 1 and an additional 0.0957gm sample) either did not produce usable data or were omitted for possible water contamination. Although $Na_{0.77}CoO_2$ studies did not result in any elastic fits, the resonant frequency peaks were of sufficient integrity to discern the temperature dependency of the elastic constants (f^2 vs T) (fig. 27).

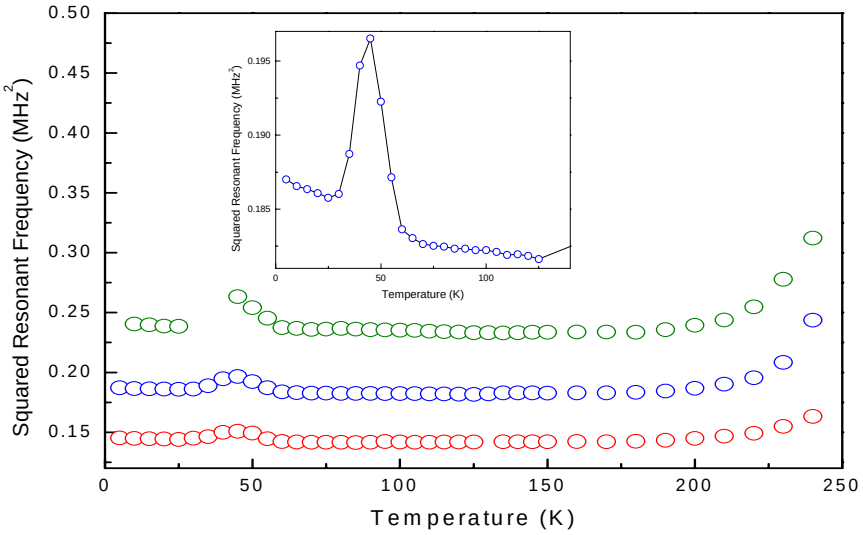

Fig. 27. Selected resonant frequencies plotted versus temperature for single crystal $Na_{0.77}CoO_2$ (sample 3). Inset: Zoom in on low temperature anomaly for one of the arbitrary frequencies.

A summary of the calculated single crystal elastic constants at 160K is provided in table 4. This temperature was chosen for illustrative purposes. Similar results have been observed across all temperatures. Reproducibility appears to be an issue as the calculated values differ quite substantially between samples for both the polycrystalline structure (table 3) and single crystal structure respectively (table 4). In spite of extensive study (31 scans), reproducibility has remained elusive as elastic fits were few.

In effort to find reproducibility where fits were sparse, attempts were made to compare the single crystal and the polycrystal data by calculating isotropic bulk and shear moduli from the single crystal values. This was done by utilizing Voigt and Reuss approximations. The Voigt approximation represents the upper limit for the calculated isotropic modulus and the Reuss approximation represents the lower limit [25]. The arithmetic mean of these two values has been suggested by Hill to be the most probable value [26]. The results as compared to the observed polycrystal values are shown in table 5. It is of little surprise that a large discrepancy exists. Both the Voigt and Reuss approximations rely on single crystal values that, as previously discussed, contain substantial error. For example, the Voigt approximation for the isotropic bulk modulus

Table 4. Single Crystal independent moduli at 160K. Units are 10^{11} Pascals. Similar results were observed for all temperatures.

	Sample 1			**Sample 2**
	0T	**5T**		**0T**
c44	0.3256	0.3196		0.3883
c66	0.8523	0.8341		0.6612

Table 5. Calculated and observed polycrystal bulk and shear moduli. Units are 10^{11} Pascals. Data presented is at 130K. Similar results were observed for all temperatures.

	calculated poly		observed poly	
	Sample 1 (single x-tal)	Sample 2 (single x-tal)	Sample 1 (poly x-tal)	Sample 2 (poly x-tal)
B_v	1.251344	0.874078		
B_r	1.124242	0.304361		
B(avg)	1.187793	0.58922		
B(obs)			0.259	0.1753
G_v	0.620847	0.516367		
G_r	0.033515	0.021467		
G(avg)	0.327181	0.268917		
G(obs)			0.1915	0.16046

(equations 8 and 9) is completely dependant on values that have been poorly determined by the single crystal fitting routine.

$$B_v = \frac{1}{9}(c_{11} + c_{22} + c_{33}) + \frac{2}{9}(c_{12} + c_{23} + c_{13}) \qquad \textit{eqn. 8}$$

$$B_v = \frac{1}{9}(2c_{11} + c_{33}) + \frac{2}{9}(c_{12} + 2c_{13}) \text{ (hexagonal symmetry)} \qquad \textit{eqn. 9}$$

Lack of confidence in the absolute values of the elastic constants makes a directional analysis of the unusual behavior of this material impossible. This is a most unfortunate result. The existing theories regarding the low temperature magnetic state and the abnormal source of thermopower are incomplete; knowledge of the elastic tensor would prove useful to constrain interpretations. An excellent example of the potential utility of the elastic tensor was provided by Santos *et al*. [27]. In this study, directional thermal expansion measurements on $Na_{0.75}CoO_2$ single crystals have displayed substantial anisotropy through the 22K transition temp. Here it was shown that the transition leads to a strain along c that is opposite to that along a. In this paper it was suggested that knowledge of the elastic tensor would enable a careful analysis of the

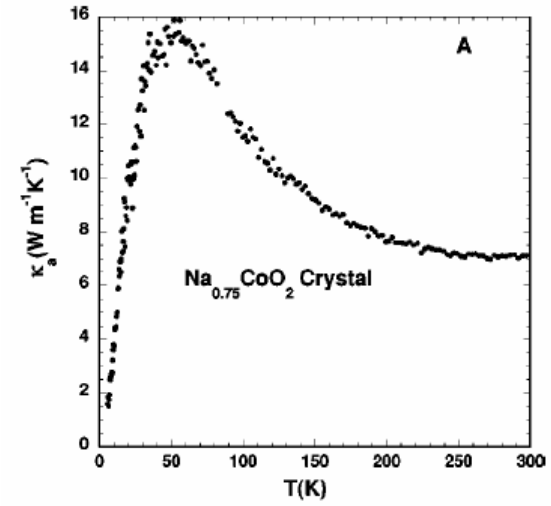

Fig. 28. In-plane thermal conductivity vs. temperature. [15]

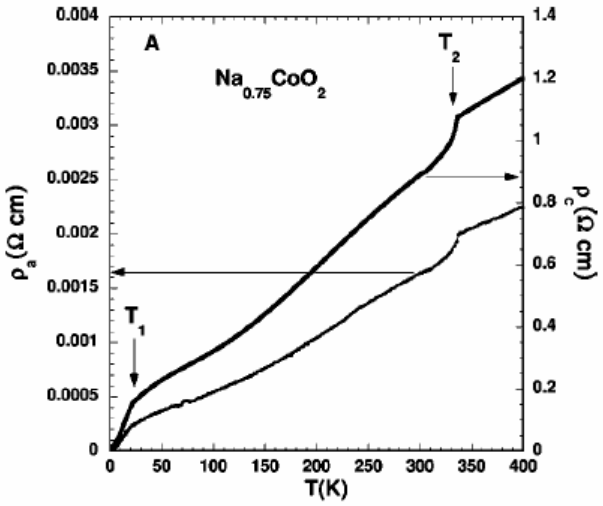

Fig. 29. Resisitivity for current in the plane (ρ_a) and along the c axis (ρ_c). Two transitions are observed (T_1 and T_2). [15]

stresses and strains and their effects on the transition temperature.

In-plane thermal conductivity has been shown to rise to a broad maximum in the low temperature range and does not pick up the 22K transition (fig. 28) [15]. Sales suggests that the lack of clear anomaly at 22K in the thermal conductivity measurements would indicate a weak coupling between the conduction electrons involved in the transition and acoustic phonons that carry most of the heat [15]. This would explain why our studies also have not detected the 22K transition.

The high temperature elastic hump lies well below the 340K order-disorder transition (fig. 29) and has not been detected by other studies. The mechanisms behind this anomaly and that of lower temperatures are unclear at this point.

CHAPTER 5: CONLUSIONS AND RECOMMENDATIONS

As the search for promising bulk thermoelectric materials intensifies, the cobalt based layered oxide Na_xCoO_2 stands out as possessing significant potential for achieving high ZT (thermoelectric figure of merit). Na_xCoO_2 has high electrical conductivity, low thermal conductivity, and an unusually large thermopower (Q). These qualities are in favor of large ZT as the figure of merit is equal to the square of Q and the ratio of electrical and thermal conductivities. Traditional thermoelectric mechanisms (charge-carrier diffusion and phonon drag) have minimal influence on Q in Na_xCoO_2 which opens the door for unconventional theories regarding thermopower. The large thermoelectric power in Na_xCoO_2 is theorized to derive from spin entropy of the charge carriers [4].

As existing theories regarding the phenomenon in Na_xCoO_2 are incomplete, we have set out to elucidate some of the issues by looking into the elastic response of the system. To this effect, we have employed Resonant Ultrasound Spectroscopy to obtain the elastic tensor at various temperatures. As the $Na_{0.75}CoO_2$ stoichiometry seemed to potentially offer the most rewards due to a pronounced ground state and anomalous thermopower at higher temperatures, this composition was chosen for study. Polycrystal samples and floating zone grown single crystal samples were studied in temperatures ranging from 5K to 300K and in various magnetic fields from 0T to 5T.

In total, thirteen samples have been studied with various magnetic fields, mounting positions, and other varying conditions. Thirty-one total runs were made in the PPMS equaling well over six-hundred hours of data acquisition alone. We believe that the low yield of quality data was a result of moisture contamination as this material is highly sensitive to water. Although ample preventative care was taken, prolonged humidity exposure during sample preparation was unavoidable. Water exposure for some samples was also a result of a temporary malfunction in the PPMS that caused a slow leak which in turn allowed moisture into the sample chamber.

Full elastic tensors were obtained for two polycrystal samples, but the absolute values of the moduli were not in sufficient agreement to conclude with confidence that they had been accurately determined. Temperature dependencies however were consistent and displayed two

regions where the material elastically deviated from “normal” behavior. Such a deviation can be interpreted as anomalous behavior and is often indicative of a phase transition. Abnormal behavior in these temperature regions however have seldom been observed in other $Na_{0.75}CoO_2$ studies (hall coefficient, heat capacity, etc…). As a result the sources of these anomalies remain unknown as there is insufficient data to hazard a guess as to what mechanisms are responsible.

Our studies of single crystal samples produced results which are very similar to that of the polycrystals. Full elastic tensors were obtained for two single crystal samples. As was the case for the polycrystal tensors, they also were not in sufficient agreement to conclude with confidence that they had been accurately determined. Temperature dependencies again displayed two regions of anomalous behavior which were similar in shape and temperature range as those found in the polycrystal samples (high T “hump” shifted slightly to higher temperatures).

Both thermopower and elasticity have been observed to be susceptible to an external magnetic field, which leads to a suppression of the thermopower and elastic softening. In this light, it would be interesting to investigate a possible connection between elasticity and thermopower to determine if these field effects are intertwined. Although Q vs. T data (fig. 26) does not show anomalous behavior that would coincide with the elastic “humps” observed in our studies, it seems a bit preemptive to rule out the possibility. Future RUS studies (with samples prepared in a very dry environment) of Na_xCoO_2 should be performed as a function of both temperature and small increments of magnetic fields through the 8T value where complete suppression of Q has been observed.

BIBLIOGRAPHY

1.) C.T. Lin, D.P. Chen, A. Maljuk, and P. Lemmens, *Journal of Crystal Growth* **292,** 422-428 (2006)
2.) L. Gao, Y. Y. Xue, F. Chen, Q. Xiong, R. L. Meng, D. Ramirez, C. W. Chu, J. H. Eggert, and H. K. Mao, *Phys. Rev.* B **50** (6), 4260-4263 (1994)
3.) Y. Ando, N. Miyamoto, K. Segawa, T. Kawata, and I. Terasaki, *Phys. Rev.* B **60** (15), 10580 - 10583 (1999)
4.) Y. Wang, N. S. Rogado, R. J. Cava, and N. P. Ong, *Nature* **423**, 425-428 (2003)
5.) M. L. Foo, Y. Wang, S. Watauchi, H. W. Zandbergen, T. He, R. J. Cava, and N. P. Ong, *Phys. Rev. Let.* **92** (24), 247001 (2004)
6.) Q. Huang, M. L. Foo, R. A. Pascal Jr., J. W. Lynn, B. H. Toby, T. He, H. W. Zandbergen, and R. J. Cava, *Phys. Rev.* B **70**, 184110 (2004)
7.) K. Takada, H. Sakaurai, E. Takayama-Muromachi, F. Izumi, R. A. Dilanian, and T. Sasaki, *Nature* **421**, 53-55 (2003)
8.) H. W. Zandbergen, M. Foo, Q. Xu, V. Kumar, and R. J. Cava, *Phys. Rev.* B **70**, 024101 (2004)
9.) F.L. Ning, S.M. Golin, K. Ahilan, T. Imai, G.J. Shu, and F.C. Chou, *Phys. Rev. Let*. **100**(086405) (2008)
10.) H. Alloul, I. R. Mukhamedshin, G. Collin, and N. Blanchard, *EPL Journal* **82**, 17002 (2008)
11.) M. D. Johannes, I. I. Mazin, and D. J. Singh, *Phys. Rev.* B **71**, 214410, (2005)
12.) N. L. Wang and J. L. Luo, *Science and Tech. of Adv. Mat.***6**, 746-749 (2005)
13.) S. P. Bayraki, I. Mirebeau, P. Bourges, Y. Sidis, M. Enderle, J. Mesot, D. P. Chen, C. T. Lin, and B. Keimer, *Phys. Rev. Let.* **94**, 157205 (2005)
14.) L. M. Helme, A. T. Boothroyd, R. Coldea, D. Prabhakaran, D. A. Tennant, A. Hiess, and J. Kulda, *Phys. Rev. Let.* **94,** 157206 (2005)
15.) B. C. Sales, R. Jin, K. A. Affholter, P. Khalifah, G. M. Veith, and D. Mandrus, *Phys. Rev.* B **70**, 174419 (2004)
16.) Y. V. Sushko, O. B. Korneta, S. O. Leontsev, R. Jin, B. C. Sales, and D. Mandrus, *Journal of Low Temp. Phys.* **142**, 577-580 (2007)
17.) S.R. Elliot, The Physics and Chemistry of Solids John Wiley & Sons Ltd. (1998)
18.) A. Migliori and J. Sarrao, Resonant Ultrasound Spectroscopy John Wiley and Sons, Inc. (1997)
19.) O.L. Anderson, D. Isaak, and H. Oda, *Rev. Geophys.* **30** (1992) 57
20.) R.G. Leisure and F.A. Willis, *J. Phys.: Condens. Matter* **9**, 6001 (1997)
21.) Gérald Bianchi, Barbara Solenthaler, Matthias Harders, and Gábor Székely, "Simultaneous Topology and Stiffness Identification for Mass-Spring Models based on FEM Reference Deformations." Department of Informatics, University of Zürich. 5 October 2008 <http://www.ifi.uzh.ch/vmml/solenthalerResearch.html>.
22.) G. Li, R Adebisi, and J. Gladden, "Four Normal Modes of a Parallelepiped." High Temperature resonant Ultrasound Spectroscopy (RUS) Methods. 5 October 2008 <http://www.phy.olemiss.edu/Colloquia/gyli_seminar.pdf>.
23.) Arkfen and Weber, Mathematical Methods for Physicits Elsevier Inc. (2005)
24.) T. Motohashi, E. Naujalis, R. Ueda, K. Isawa, M. Karppinen, and H. Yamauchi, Appl. Phys. Let. **79**, 1480 (2001).

25.) E. Schreiber, O. Anderson, and N. Soga, Elastic Constants and Their Measurements McGraw Hill, Inc. (1973)
26.) R. Hill, *J. Phys. Chem. Soc.*, **24**, 909 (1963)
27.) C.A.M. dos Santos, J.J. Neumeier, Yi-Kuo Yu, R.K. Bollinger, R. Jin, D. Mandrus, and B.C. Sales, *Phys. Rev.* B **74**, 132402 (2006)

VITA

Timothy Cagle was born in Metairie, Louisiana in September of 1980. He received a Bachelors degree in Electrical Engineering from Louisiana State University in the spring of 2003. He then moved to Knoxville, Tennessee where he studied Materials Science and Engineering at the University of Tennessee.